

Single-Step Fabrication Method toward 3D Printing Composite Diamond–Titanium Interfaces for Neural Applications

Nour Mani, Arman Ahnood, Danli Peng, Wei Tong, Marsilea Booth, Alan Jones, Billy Murdoch, Nhiem Tran, Shadi Houshyar, and Kate Fox*



Cite This: *ACS Appl. Mater. Interfaces* 2021, 13, 31474–31484



Read Online

ACCESS |



Metrics & More



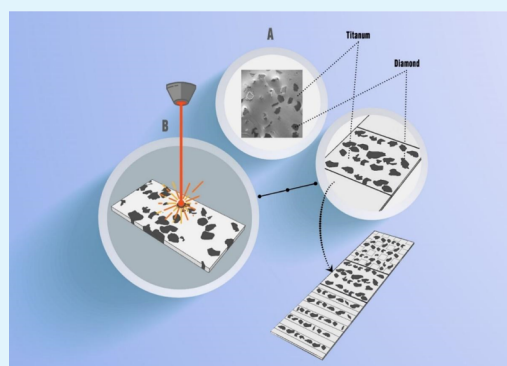
Article Recommendations



Supporting Information

ABSTRACT: Owing to several key attributes, diamond is an attractive candidate material for neural interfacing electrodes. The emergence of additive-manufacturing (AM) of diamond-based materials has addressed multiple challenges associated with the fabrication of diamond electrodes using the conventional chemical vapor deposition (CVD) approach. Unlike the CVD approach, AM methods have enabled the deposition of three-dimensional diamond-based material at room temperature. This work demonstrates the feasibility of using laser metal deposition to fabricate diamond–titanium hybrid electrodes for neuronal interfacing. In addition to exhibiting a high electrochemical capacitance of 1.1 mF cm^{-2} and a low electrochemical impedance of $1 \text{ k}\Omega \text{ cm}^2$ at 1 kHz in physiological saline, these electrodes exhibit a high degree of biocompatibility assessed *in vitro* using cortical neurons. Furthermore, surface characterization methods show the presence of an oxygen-rich mixed-phase diamond–titanium surface along the grain boundaries. Overall, we demonstrated that our unique approach facilitates printing biocompatible titanium–diamond site-specific coating-free conductive hybrid surfaces using AM, which paves the way to printing customized electrodes and interfacing implantable medical devices.

KEYWORDS: diamond, laser metal deposition, biocompatibility, electrochemistry, neuronal interface



1. INTRODUCTION

Neural interfaces are an emergent research field that captures the nervous system interactions with medical devices. Accordingly, researchers can neuro-engineer medical systems that translate the observed data into clinically relevant advances.¹ Primarily, neural interfaces are critical to record, analyze, and restore patients with vision or brain damage and neurodegenerative diseases. Moreover, neural interfaces include electrodes used fundamentally to selectively stimulate or record neural activities (unidirectional) and connect the nervous system to the outside world. Advanced therapeutic opportunities also include closed-loop systems, which exist as bidirectional sensory devices.^{2,3} However, the neural system's complexity requires continuously innovating the design, fabrication, and body-device integration systems to meet the needed functions. Hence, new manufacturing technologies such as additive manufacturing (AM) are considered key to overcome these challenges.⁴

AM allows the production of complex shapes via computer-aided design (CAD) files used for printing layer-by-layer of deposited materials. The driving force to use AM in implant engineering is the freedom of design it offers, the short time to market, and the ease to use powders.⁵ In general, AM facilitates the printing of reliable high-performing parts with specific

geometries and different thicknesses. AM techniques are classified into multiple categories, including laser metal deposition (LMD), powder bed fusion, sheet lamination, direct material melting, including fused deposition modeling, binder jetting, material jetting, and vat photopolymerization.

Multiple AM or 3D printing techniques have been investigated to fabricate electrochemical cells or analytical devices. Previously, the possibilities of producing conductive electrodes such as polylactic acid–graphene electrodes and fabricating sensing platforms via 3D printing have been investigated.⁶ Though LMD is less discussed as a printing technique for electrochemical purposes, it facilitates printing geometry-specific surfaces using metal powders. Nevertheless, the powders need to be optimized and explicitly designed to be used in medical applications to ensure they match the body's requirement. Although titanium is regularly used in implant fabrication,^{7,8} it requires surface modification techniques such

Received: April 21, 2021

Accepted: June 17, 2021

Published: June 30, 2021



as coatings to interact with the body successfully. Nevertheless, coatings suffer from degradation, delamination, and cracking due to the resulting strain caused by the implant-tissue mechanical mismatch.⁹ Hence, the next generation of electrode material is required to have advanced capabilities such as unique architectures, chronic stability, biocompatibility, and optimal mechanical and electrochemical properties. This signals the need to develop advanced powders with enhanced functionalities, such as the newly developed powder, titanium–diamond composite powder.¹⁰

Diamond is one of the most attractive materials used in bio-electrochemistry and bio-interfacing due to its combination of key characteristics such as biocompatibility, long-term response, and selective conductivity.^{11,12} The face-centered cubic's crystal structure of diamond provides high chemical and physical stability. The carbon atoms are sp^3 hybridized with a C–C bond length of 1.54 Å and are tetrahedrally arranged.¹³ The short-range carbon bonds and the atoms' organization determine the characteristic chemical, physical, and electrochemical properties of diamond. In its intrinsic form, diamond exhibits very high resistivity, rendering it unusable for many electrochemical applications. Traditionally, this has been commonly addressed through doping with different elements such as boron, nitrogen, phosphorous, sulfur, and arsenic.^{14–16} So far, boron-doped diamond is the most extensively used diamond in electrochemistry due to its high conductivity. The processes of chemical vapor deposition synthesis and boron doping (*in situ* and *ex situ*) are mainly utilized for the fabrication of thin films. Alternatively, the incorporation of graphitic grain boundaries into the diamond structure increases the conductivity. Many reports detail sufficient conductivity without doping and present the electrical properties influenced by the surface functionalization and crystalline quality of the diamond material.^{17,18}

The rich carbon structure of diamond allows diamond functionalization by multiple methods, mainly by either hydrogen or oxygen, to control surface reactivity and properties. The functionalization method affects the electrical conductivity of the surface and energy states due to opposite dipoles C–H and C–O.¹⁹ For instance, diamond surfaces are oxygen-functionalized using different functionalization methods such as oxygen plasma treatment, wet/dry chemical treatments (e.g., boiling in strong acid), or electrochemical oxidation.^{20,21} Oxygen-functionalized surfaces usually have lower energy levels relative to the vacuum level. Along with these interesting features, oxygen-functionalized surfaces develop hydrophilic properties.^{11,22,23} In addition, oxygen functionalized surfaces reportedly enhance cell attachment and create a favorable environment for cell growth and biological interaction.^{24–26} As such, oxygen functionalization allows controlling the material surface wettability and consequently enhancing its biocompatibility which is favorable in implant engineering. Moreover, surface treatment such as oxygen plasma results in faster etching of sp^2 graphitic impurities and exposing the rich sp^3 surface of the material.²⁷ This is particularly important as it enables better observation of the sub-features of the surface and facilitates optimizing the etching process to customize the electrochemical performance of the material.²⁸

Here, we report the feasibility of using LMD as an effective technology for directly printing conductive surfaces. We investigate the electrochemical properties of a new titanium–diamond (TiD) material to understand the capability of the

hybrid material and its suitability to perform as a potential electrode or neural interface. The new material offers biocompatibility and electrical properties comparable to the current electrodes. Furthermore, the fabrication using LMD provides the flexibility to build different geometries of TiD interfaces and devices that can sustain a demanding environment such as the human body and provide long-term stable function with minimum material waste.²⁹ This combination of properties was not previously achieved using conventional materials and methods. This work builds upon our previous work, where we developed the manufacturing process for the novel TiD composite material using LMD.¹⁰

3D printing diamond using LMD has proved challenging for new and hybrid materials due to limitations in both powder size and the need for the powders to efficiently flow through the print nozzle. We have worked toward overcoming this challenge by investigating the optimum printing process. As a result, our work defined the printing strategy (per diamond ratio) that allows successful printing of high integrity parts and has led us to the selection of specific powder ratios of TiD (30 and 50%) to provide sufficient demonstration of the process effectiveness and a significant electrochemical difference along the gradient of properties. Furthermore, as reported previously,¹⁰ TiD in a 50:50 ratio provides the best ratio for mammalian cell proliferation. Anything above 50% diamond does not effectively flow through the nozzle. Hence, the printed TiD was loaded with up to 50% microdiamond while providing a biocompatible printed material; however, its capacity to form an electrode material remains unreported. Herein, we present the effect of compositional changes on the electrochemical properties of TiD fabricated using LMD. The *in vitro* biocompatibility of the functionalized TiD was assessed using primary rat cortical neurons. Specifically, this study provides a single-step method to print a diamond-titanium (coating-free) surface with desirable electrochemical and biocompatible properties capable of neuronal cell adhesion.

2. MATERIALS & METHODS

2.1. Powder Preparation. Titanium (Ti-6Al-4 V) powder (TLS, Germany, ASTM Gd5 ELI powder 45–90 μm) was mixed with as-received 50 μm micro-diamond powder (Microdiamant, Germany) for 1–3 h in a Turbula mixer to ensure powder homogeneity.

2.2. Single-Step Fabrication. The samples were additively manufactured into $5 \times 5 \times 2 \text{ mm}^3$ planar parts using a TRUMPF TruLaser Cell 7020 LMD as reported previously.³⁰ The system was equipped with a 3.0 kW disk laser, coaxial laser cladding head (focal length 200 mm), and coaxial powder delivery system (focal distance 8.0 mm). TiD samples were categorized according to their diamond concentration and labeled TiD₅₀ (50% diamond powder) and TiD₃₀ (30% diamond powder).

2.3. Sample Characterization. Topographical imaging was performed using a scanning electron microscope (Quanta 200-SEM) with an Oxford X-Max20 E.D.X. detector at an acceleration voltage of 30 kV in a high vacuum mode with a spot size of 5 μm and a working distance of 10 mm. X-ray photoelectron spectroscopy (XPS) (Thermo Fisher K-Alpha) was used to obtain the oxygen-functionalized chemical composition of the TiD samples with an Al K α radiation source at a power of 300 W. The spot size of analysis was 400 μm . Sample scanning was performed using the flood gun function to compensate for charging and the auto height function to determine the optimal distance for the X-ray beam and the sample. The elements detected in the surface layers (analysis depth 2–5 nm) were observed from the survey spectrum (pass energy 200 eV) over a range of 0–1100 eV (step size 1 eV, dwell time 50 ms). The XPS binding energy values were obtained from the high-resolution scans of

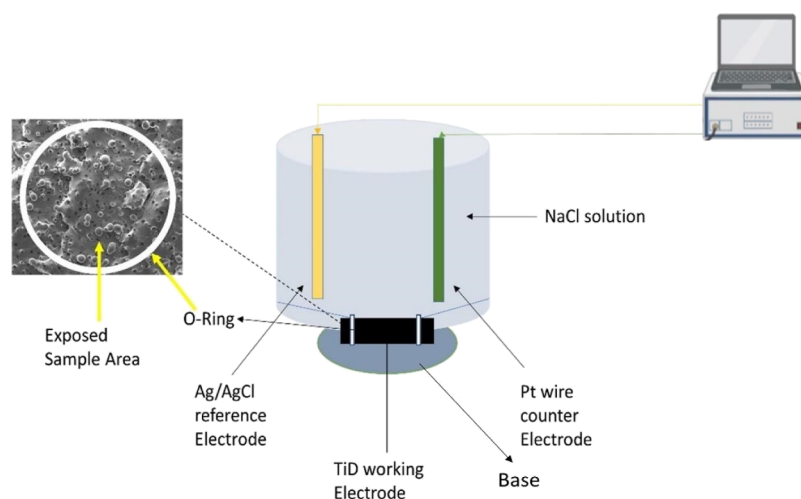


Figure 1. Principle of CV electrochemical 3D printing setup showing the use of an O-ring (illustrated as a white circle) to control the exposed surface of the LMD TiD.

elemental signals (pass energy 50 eV). They were not charge-corrected with respect to that of adventitious carbon at 284.8 eV due to the scanning being undertaken using the flood gun. The high-resolution XPS spectra were collected for the critical elements carbon, oxygen, and titanium, as identified from the survey spectra. High-resolution scanning was undertaken with a step size of 0.1 eV and a dwell time of 50 ms.

The measurement of the 3D roughness of the top surfaces of TiD was carried out using a Stylus Profiler (KLA Tencor, Inc.) with a 1 mg force and a scan rate of 10 $\mu\text{m/s}$ over an area of 1000 μm . Five measurements in total were performed per sample category across the surface area. The average of measurements was used to represent the surface topography.

2.4. Electrochemistry Measurement. Oxygen plasma treatment and functionalization was achieved using a Diener Femto plasma cleaner, with a 3:1 argon:oxygen plasma with a power of 50 W for 3 h. The electrochemistry was performed in a three-electrode setup using a Gamry potentiostat (Interface 1000E) as illustrated in Figure 1. A Ag/AgCl electrode and a Pt wire counter electrode were used as the reference and counter electrode, respectively. The cell chamber contained physiological saline solution (0.1 M NaCl solution in deionized water). The TiD samples were used as the planar working electrodes and cleaned with acetone using an ultrasonic bath before experiments. Cyclic voltammetry (CV) of functionalized samples was performed over a potential range of -0.5 V to 0.5 V versus Ag/AgCl, with scan rates ranging from 20 to 500 mV/s. The capacitance was calculated according to the relationship $I = C \left(\frac{dv}{dt} \right)$, where I is the current (A), C is the capacitance (F), and dv/dt is the scan rate (V/s).³⁰ The specific electrochemical capacitance (C_p) was extracted from CV measurements by recording the current width at 0 V for different scan rates ($n = 3$ per group). Later, the slope of the resultant fitted plot was calculated and divided by the electrode's exposed area to the saline solution (0.031 cm^2). The charge injection capacity (CIC) is the amount of charge injected into the electrode within the potential safe window and without exceeding the highest safe voltage. The maximum charge value is given by $Q = C \cdot V$ where Q is the charge (C), C is the capacitance (F), and V is the maximum safe voltage.³¹ In this study, the CIC was calculated by multiplying the specific capacitance by the highest voltage within the potential range (-0.5 to $+0.5$ V), which is 0.5 V. Electrochemical impedance spectroscopy was measured over a frequency range of 0.2 Hz to 100 kHz with an AC signal of 10 mV amplitude relative to the open-circuit potential.

2.5. Primary Cortical Neuron Culture Studies. All experimental procedures conformed to the National Health and Medical Research Council of Australia (NHMRC) and were approved by the Animal Experimental Ethics Committee of the University of

Melbourne (ethics approval #1814396). The functionalized TiD samples were sterilized using an autoclave and then placed in a 24-well dish. Coverslips coated with 0.05 mg/mL poly-D-lysine were used as the control. Primary rat cortical cultures were obtained by isolating the cerebral cortices from 1 day old rats. Briefly, the heads were removed and placed in Hank's balanced salt solution (HBSS). Then, the skin and top of the skull were removed and a small area of the cortex was pinched off with fine forceps. Meninges were removed and the tissue was chopped with a scalpel blade. The tissue was dissociated by protease digestion for 20 min at 37 $^{\circ}\text{C}$ using 10 $\mu\text{g/mL}$ DNase 1 and 250 $\mu\text{g/mL}$ trypsin in HBSS. Trypsinization was terminated using Soybean Trypsin Inhibitor (Sigma) containing 10 $\mu\text{g mL}^{-1}$ DNase 1, and the cells were pelleted by centrifuging and triturated using a P1000 pipette. The cells were diluted in culture medium (Neurobasal A with 2% B27 supplement, 2 mM Glutamax, 100 $\mu\text{g/mL}$ penicillin, and 100 $\mu\text{g/mL}$ streptomycin). Finally, the cells were seeded on all samples at a density of 40,000 cells per well. The cell cultures were incubated at 37 $^{\circ}\text{C}$ in 5% CO_2 . Half of the culture medium was replaced after 24 h of cell seeding.

After 4 days of incubation, the samples were washed with phosphate-buffered saline (PBS), then fixed in 4% paraformaldehyde in PBS for 10 min at room temperature, followed by cold (-20 $^{\circ}\text{C}$) methanol for another 10 min. After washing with PBS three times, the samples were incubated in a blocking solution (2% fetal calf serum and 2% normal goat serum in PBS) for 30 min. The samples were then incubated for 20 min with the primary antibody (mouse anti-beta-III tubulin) at room temperature, followed by the PBS wash; the samples were incubated with the secondary antibody (Alexa 488-conjugated goat anti-mouse immunoglobulin) and propidium iodide. They were finally washed with PBS and imaged using a confocal microscope (Olympus, FV 1200). Images were obtained using an excitation laser at either 473 or 532 nm through a Nikon Plan Apo 0.75-numerical aperture $\times 20$ objective. Data analysis was performed from at least 15 images collected from each sample group. Neuron coverage was analyzed in Matlab (MathWorks, Boston MA). Neurite analysis was done by a Neurite Analyzer in Fiji.³² Statistical analysis was performed using a GraphPad Prism.

3. RESULTS AND DISCUSSION

3.1. TiD Surface Morphology. Figure 2 shows a scanning electron micrograph of the LMD samples. In each micrograph, the micro-diamond particles are visible, with diamond particles more prevalent as expected in the TiD₅₀ samples (Figure 2a). The images display additive material surface integrity following LMD and the inherited surface morphology resulting in dense titanium unmelted particles.³³

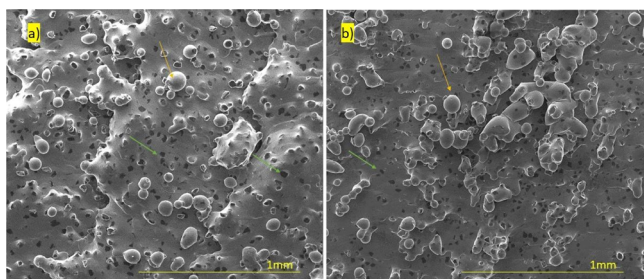


Figure 2. (a) SEM micrographs of TiD₅₀ with 50% diamond and (b) TiD₃₀ with 30% diamond. The green arrows represent embedded diamond particles and the dense population of titanium unmelted grey particles is represented by the yellow arrows on both surfaces.

3.2. TiD Surface Roughness. Maximum peak height (Rp), maximum valley depth (Rv), the arithmetic average of roughness profile (Ra), and root mean square deviation of the roughness profile (Rq) are critical surface profile parameters that reflect the surface morphology properties resulting from the optimized printing parameters and provide a guided pathway for further development. TiD samples comprising 50% diamond show average peak heights of 74.51 μm and an average depth of the valley of 35.11 μm . For TiD comprising 30% diamond, the average peak height (Rp) is 41.47 μm and the average depth of the valley (Rv) is 36.04 μm . The increase in the average peak height and valley depth in TiD₅₀ can be attributed to the overlapping scanning paths, leading to the special surface finish and wide unmelted titanium particles on the surface, as shown in Figure 2.³³ Ra and Rq for the samples are shown in Table 1. We observe that Ra and Rq values

Table 1. Average Surface Profile Properties Obtained by a Profilometer for Five Consecutive Scans of the Samples Determining Averages of Maximum Peak Height (Rp), Maximum Valley Depth (Rv), the Arithmetic Average of Roughness Profile (Ra), and Root Mean Square Deviation of the Roughness Profile (Rq) Showing That the Surface Roughness Increases with the Diamond Concentration

roughness (μM)	Ra	Rp	Rv	Rq	Rku
TiD ₅₀	24.25	74.51	35.11	28.58	1.9
TiD ₃₀	20.88	41.47	36.04	24.00	2.3

increase with the increase in diamond concentration. The highest Ra (24.25 μm) and Rq (28.58 μm) values have been

associated with the higher diamond concentration. This highlights that printing conditions optimization is a critical factor to control the inherited surface morphology. Another critical factor to investigate is the Kurtosis (Rku) which reflects the sharpness of the surface's primary profile; all samples had a kurtosis of less than 3 ($Rku < 3$), indicating that the surface is showing less sharp and more squashed peaks and valleys.³⁴ It was interpreted as indicating that the additive manufactured surface is less likely to initiate a crack.

3.3. TiD Surface Chemistry Study. Figure 3 shows the XPS spectra of the two LMD oxygen-functionalized diamond samples. The figure confirms the presence of diamond within the TiD matrix after LMD showing that the high-resolution carbon XPS spectra of the TiD surface resolved into multiple carbon chemical forms. Diamond has sp^3 hybridization with a C–C bond peak at ~ 285 eV, whereas graphite has sp^2 hybridization in the C–C bond with a peak at ~ 284 eV.^{35–37} All samples display the sp^3 diamond peak at ~ 285 eV and sp^2 graphitic impurities C–C peak at ~ 284 eV.

The XPS suggests the dense formation of C–O and C=O bonds on the samples' surface. It displays similar peak shapes with the amount of C–O bonds yielding a relative percentage of 23.30 and 14.49% for TiD₅₀ (50% diamond) and TiD₃₀ (30% diamond), respectively. The higher C–O contribution is associated with the increased percentage of diamond (50%) and is approximately 1.6 times the value of the C–O bond associated with the 30% diamond volume fraction. The small sp^2 content shown in the XPS can be attributed to graphitic impurities.³⁸ To accurately ascertain the oxygen change on the different LMD surfaces, the total oxygen/carbon ratio was compared, as shown in Table 2. The precise peak

Table 2. Diverse Carbon Components and the Corresponding Percentages of the Hybrid TiD Sample Surfaces

O ₂ plasma 3 h	sp^2 %	C–O %	sp^3 %	C=O %
TiD ₅₀	3.40	23.30	67.00	6.30
TiD ₃₀	2.36	14.49	77.65	5.50

deconvolution assists in a better understanding of the oxygen-rich surface properties. The area ratio of oxygen to carbon (O/C) was estimated directly from the oxygen-related chemical components covering the TiD surface. The oxygen to carbon area ratio of AO_A/AC_A on the surface of TiD₅₀ is approximately 15%, which is higher than the AO_B/AC_B on the

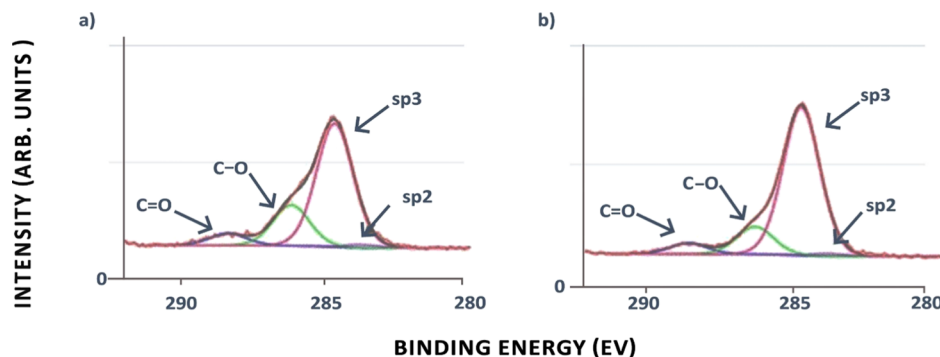


Figure 3. Chemical composition of the additively manufactured titanium–diamond composite TiD (a) shows the high-resolution C 1s (carbon) XPS spectra of TiD₅₀ showing peaks fitted for sp^2 , sp^3 , C–O, and C=O and (b) shows the high-resolution C 1s (carbon) XPS spectra of TiD₃₀ (30% diamond) showing the deconvoluted peaks fitted for sp^2 , sp^3 , C–O, and C=O bonds.

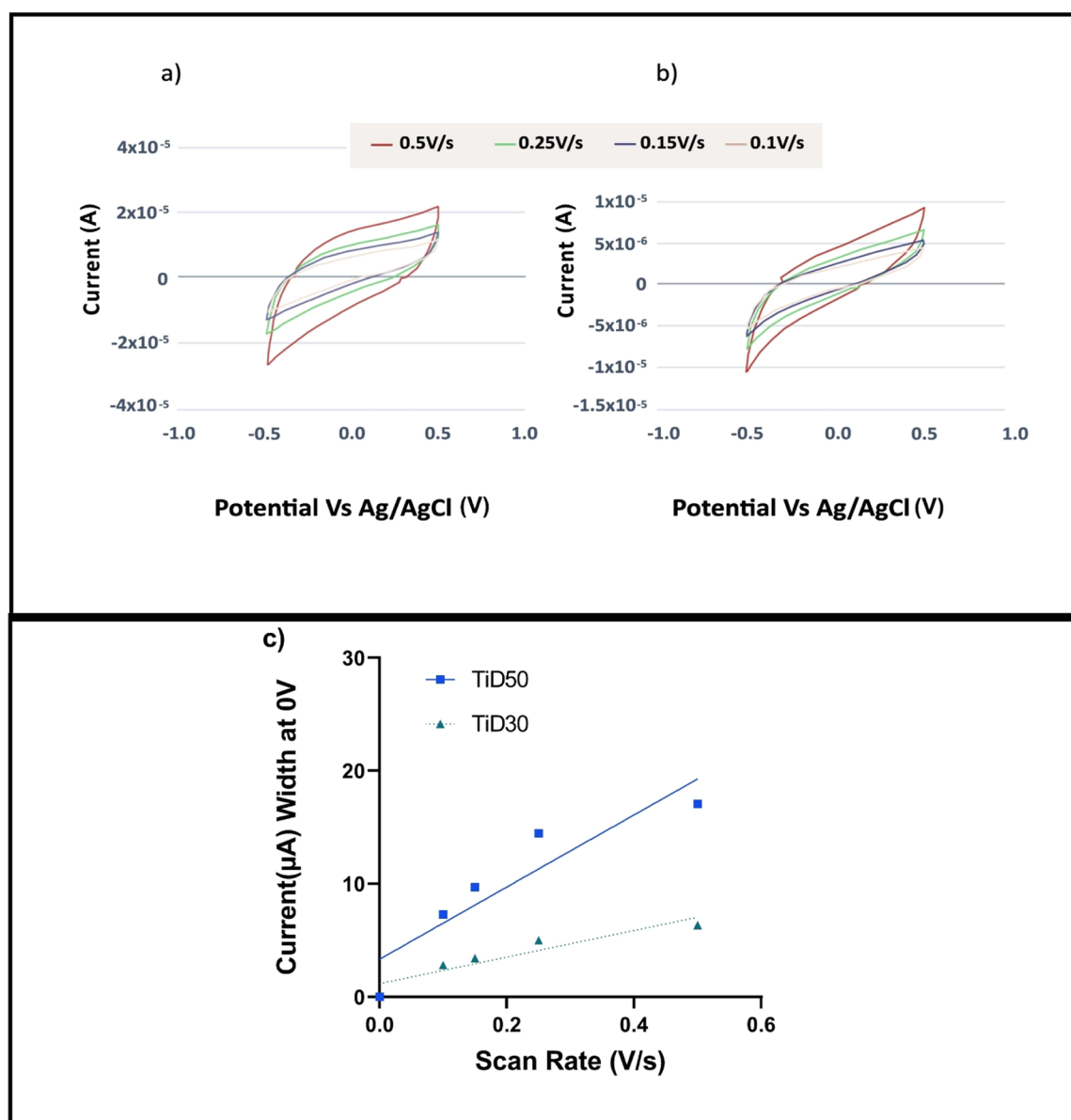


Figure 4. Voltammograms of the TiD samples. The TiD CV voltammograms in (a) TiD₅₀ and (b) TiD₃₀ present well-defined shapes. Moreover, the voltammograms demonstrate the dependence of CV on the scan rate, as the currents increase with the increase of the scan rate. (c) Current width at 0 V for both TiD₅₀ (A) and TiD₃₀ (B).

surface of TiD₃₀ with a ratio of 10%. The difference between the O/C ratios demonstrates that the diamond concentration affects the number of oxygen-related components formed on the surface.

3.4. Electrochemical Characterization of TiD. CV is a standard method used to analyze the electrochemical properties of materials. During CV, a potential is applied to the working electrode (material of interest) and changed linearly with time, starting from an initial potential and then switching the potential back to the initial value. Figure 4 shows the cyclic voltammograms of the TiD samples. Measurements were performed within the window of -0.5 to 0.5 V to avoid the oxidation/reduction processes. We observed that TiD₅₀ displays a larger enclosed area indicating a larger electrochemical capacitance than TiD₃₀. The results herein align with the previous literature, which explored the effect of oxygen functionalization on the capacitance and electrical conductivity of materials with high diamond concentration.³⁹

The current was recorded at 0 V for different scan rates and the specific electrochemical capacitance (C_p) of the TiD samples was calculated according to the slope of the linear fitting divided by the exposed area, as shown in Figure 4. C_p is the specific electrochemical capacitance and GSA is the geometric surface area of the electrode exposed to the solution (0.031 cm^2). The CIC was calculated by multiplying C_p with the highest voltage (0.5V). The derived electrochemical values for the TiD samples are presented in Table 3.

Table 3. Electrochemical Properties of Hybrid TiD Presented by Specific Capacitance (C_p) and Charged Injection Capacity Values of Each Group

sample name	specific capacitance C_p ($\mu\text{F cm}^{-2}$)	CIC ($\mu\text{C cm}^{-2}$)
TiD ₅₀	1053 ± 166	526 ± 30
TiD ₃₀	430 ± 74	215 ± 35

Table 4. Range of Commonly Used Electrode Materials Compared to TiD

material type	C_p $\mu\text{F cm}^{-2}$	CIC mC cm^{-2}	impedance at 1 KHZ $\text{k}\Omega$	water window (V)	examples of biocompatibility	ref
N-UNCD nitrogen included ultrananocrystalline diamond	1	1	1	-1.1–1.1	supported healthy neuron growth	30
PT platinum		0.15–5.57	54	-0.8–0.8	electrical excitation of the nervous system	44
PT Ir		0.3		-0.6–0.7	electrical excitation of the nervous system	44,45
Gold		0.022	36.54 ± 0.88		neural interface electrode, multi-electrode neural arrays	46
IrOx		4		-0.6–0.7	thin films are unstable and prone to degradation	45
TiD ₅₀	1	0.53	0.75 ± 0.07	-0.8–0.8	the material proves to be non-cytotoxic as neurons survived and proliferated on the surface	this work
TiD ₃₀	0.43	0.22	0.55 ± 0.03	-0.8–0.8		this work

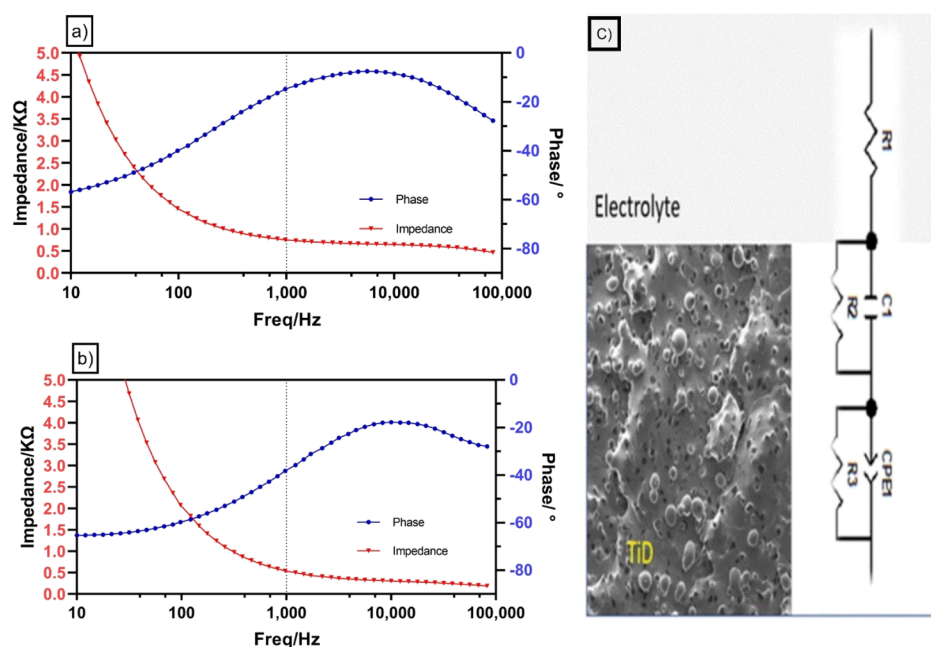


Figure 5. (A) EIS data for TiD₅₀ (50% diamond) and (B) TiD₃₀ (30% diamond), displaying increasing low-frequency impedance and a decrease in the phase angle and (c) suggested electrochemical circuit used to model the EIS data.

TiD₅₀ with 50% diamond in the hybrid sample exhibits a capacitance value of $1053 + 166 \mu\text{F cm}^{-2}$. Upon changing the diamond concentration to 30%, we note the capacitance decreases to a value of $430 \pm 74 \mu\text{F cm}^{-2}$. As a result, the CIC values are $526 \mu\text{C cm}^{-2}$ and $215 \mu\text{C cm}^{-2}$ for TiD₅₀ and TiD₃₀, respectively. These values are very high and comparable to other diamond electrodes, such as the N-UNCD electrodes with a CIC value of 1 mC cm^{-240} and the iridium oxide electrode with a charge value of $4 \text{ mC cm}^{-2,41-43}$ as presented in Table 4.

Interestingly, TiD possesses unique electrochemical properties due to being additively manufactured to form a composite surface with controlled chemical composition and volume fraction of diamond to titanium. We notice the oxygen dense surface via the high percentage of C–O and C=O oxygen functional groups on both the TiD surfaces, as confirmed by XPS data in Figure 3. The surface functionalization and etching of graphitic impurities have led to differences in electrochemical behavior.³⁰ TiD₅₀ exhibits a denser surface of oxygen functional groups with C–O and C=O values of 23.30 and 6.30%, respectively, compared to TiD₃₀ (14.49 and 5.50%). It was reported previously that oxygen functional groups enhance the electrochemical capacitance due to an increased number of

functional groups on the surface facilitating a higher charge transfer. These results are consistent with the previous studies.⁴⁷⁻⁴⁹

Additionally, XPS data demonstrate that TiD₅₀, with a higher percentage of diamond fraction (50%) and oxygen functional groups, had a higher C_p value ($1053 \pm 166 \mu\text{F cm}^{-2}$) compared to TiD₃₀, which has a lower percentage of diamond fraction (30%) and oxygen functional groups and hence, a lower C_p value of $430 \pm 74 \mu\text{F cm}^{-2}$. Consequently, TiD₅₀ has a higher CIC value ($526 \mu\text{C cm}^{-2}$) than TiD₃₀ ($215 \mu\text{C cm}^{-2}$). Specifically, the conductivity of diamond is influenced by the charge transfer along the boundary and *via* the grains and increases with the increase in diamond concentration and the number of oxygen functional groups on the surface. It is evident that the electrochemical properties continued to increase with diamond concentration due to the rich sp^3 surface and dense functional groups. The improvement can also be attributed to the graphitic diamond grain boundary regions' etching following oxygen treatment. Conversely, the metal volume fraction in the additive part is an important factor influencing conductivity, as it creates charge transfer paths.⁵⁰ The roughness, influenced by the area of unmelted titanium metal particles, increases the printed materials total

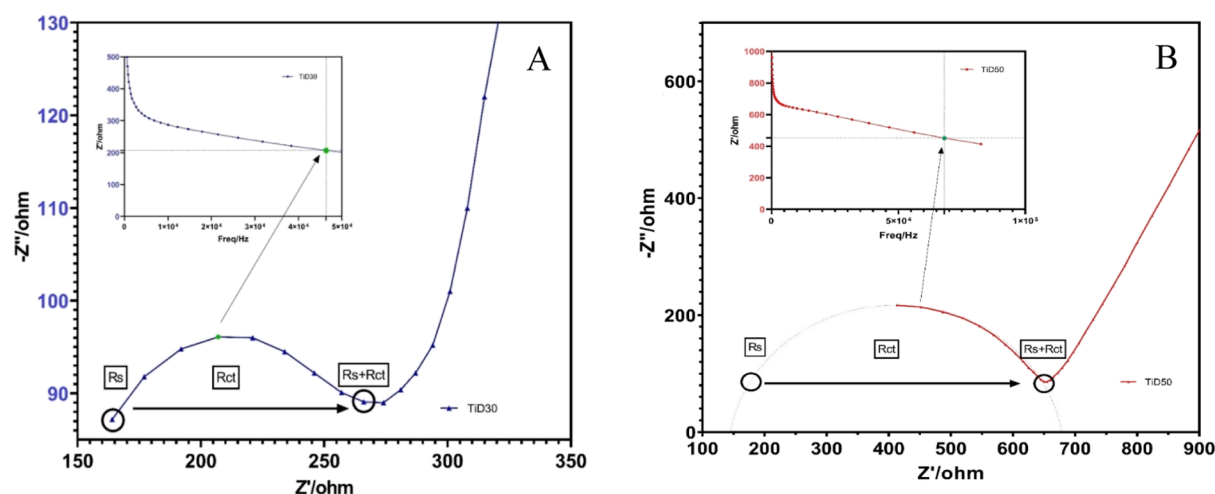


Figure 6. Nyquist plots of the TiD samples showing R_s and R_{ct} . (A) Nyquist plot for TiD₃₀ and (B) Nyquist plot for TiD₅₀.

surface area, consequently affecting the total electrochemical surface area.^{51–54} Hence, the increase in roughness will increase charge pathways and, therefore, an increase in the Cp and CIC on the TiD surface, as reported in Table 3. TiD₅₀ has a higher Ra (24.25 μm) compared to TiD₃₀ (20.88 μm) and higher Cp (1053 \pm 166 $\mu\text{F cm}^{-2}$) compared to the sample with less diamond (430 \pm 74 $\mu\text{F cm}^{-2}$).

The previous observations suggest that the possible mechanism for charge transfer over the composite surface is influenced by multiple factors, including charge transfer depending on crystal defects and the conductivity of each diamond particle as well as a particle-to-particle charge transfer.⁵⁵ Moreover, the charge paths created by the metal volume fraction within each experimental group facilitate charge transfer over the surface. Further experiments are planned to understand this physical process, leading to the differences in the overall electrochemical behavior.

Figure 5 displays the electrochemical impedance spectroscopy (EIS) studies of TiD and provides a better understanding of the material behavior over a wide frequency range. It is evident that both the sample groups exhibit similar electrical behavior and show increasing low-frequency impedance.

In order to understand the electrochemical behavior and predict TiD performance as a neural interfacing material, we have investigated the impedance at 1 kHz. Generally, low-impedance electrodes lead to low noise levels, as they require low power consumption to perform effectively. Hence, materials with lower impedance are favorable for recording applications. Additionally, materials with combinations of low impedance and high CIC values emerge as reliable candidates for stimulation applications.^{56,57} Interestingly, both the samples exhibit a low impedance at 1 kHz (TiD₅₀ 0.75 \pm 0.07 k Ω and TiD₃₀ 0.55 \pm 0.03 k Ω) and a relatively high CIC, as shown in Table 3. An implication of this is the possibility to deploy TiD in neural application successfully.

A suggested an equivalent circuit model for TiD has been proposed (Figure 5c) after fitting the EIS data. The model is expressed by R_s (R_1) as the electrolyte resistance, followed by C1, and R_{ct} (R_2) sub-circuit in series to describe the capacitance and surface charge movement resistance on the electrode/electrolyte interface as a complete Randles circuit. A constant phase element CPE was added in parallel with R_3 to compensate for TiD structural defects.⁵⁸ EIS fitting is added in Supporting Information, Figure S1.

The Nyquist plots provide details of the solution resistance R_s , the charge transfer resistance R_{ct} , the angular frequency ω , and the double layer capacitance C_{dl} . With reference to equation ($\omega R_{ct} C_{dl} = 1$),⁵⁹ we have calculated R_{ct} and R_s values for both the samples at Point Z' max (labeled in green) as shown in the table below. The TiD₅₀ sample has a longer RC time constant compared to TiD₃₀. This is consistent with the equivalent circuit parameters extracted from the Nyquist plot (see Figure 6A,B). TiD₅₀ exhibits a double layer capacitance of 1035 μF , compared to 430 μF in the case of TiD₃₀. The series resistance in both the samples is similar with the values of 164 and 140 Ohms. However, there is a significant difference between the R_{ct} values. This signifies the resistance to charge transfer—the TiD₅₀ exhibits a higher R_{ct} value of 550 Ohms compared to TiD₃₀ with the value of 93 Ohms. The higher TiD₃₀ R_{ct} can be attributed to a higher diamond concentration at the electrode–electrolyte interface—as shown in Figure 2. The combination of higher R_{ct} and C_{dl} is in line with the observed longer time constant (Table 5). A different Nyquist plot is added in Supporting Information, Figure S2.

Table 5. Values of R_s and R_{ct} as Extracted from Nyquist Plots

	R_s (Ω)	R_{ct} (Ω)	C_{dl} (μF)
TiD ₃₀	164	93	430
TiD ₅₀	140	550	1035

3.5. Assessment of Biocompatibility and Neural Cell Adhesion and Growth. Figure 7 shows the representative images obtained from different sample groups. The cells were healthy on TiD₅₀, TiD₃₀, and the control (poly-D-lysine coated polystyrene), with many neurites extruding from the soma. The results are summarized in Figure 8. According to the results, the cell density showed no significant difference between the three sample groups (Figure 8a). An analysis was also performed to examine the probability of cells forming clusters (Figure 8b). The surfaces that are more biocompatible tend to have clusters with a fewer number of cells. According to Figure 8b, TiD₅₀ showed a larger portion of cells without clustering (*i.e.*, one neuron) than TiD₃₀ and the control. Figure 8c–e quantifies the neuritogenesis of the images. The coverage of neurons showed no statistical difference between different sample groups (Figure 8c). Among the samples, the control

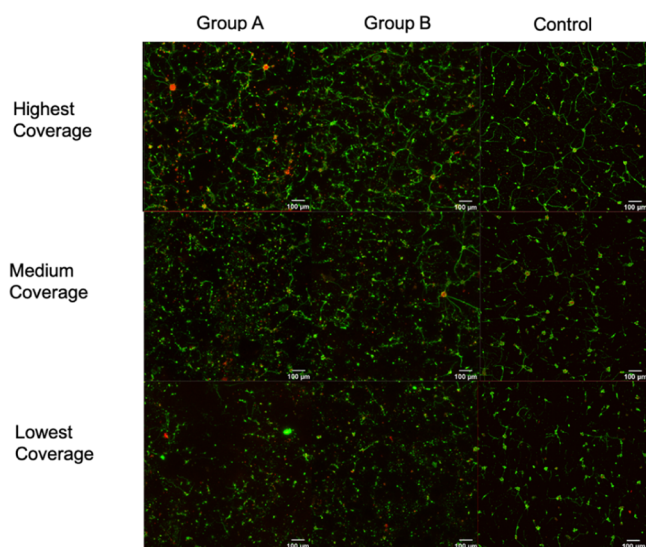


Figure 7. Representative images of neurons on different samples. Images with different coverage (highest, medium, and lowest) are shown in each row. The cells survived well on group A (TiD₅₀), B (TiD₃₀), and the control, with neurites extending from the soma. Green: beta-III tubulin (neurite). Red: propidium iodide (nuclei).

group has the most significant number of neurites per neuron and the most extended neurites (Figure 8d,e). However, TiD₃₀ showed more neurites per neuron and longer neurites than the neurons in TiD₅₀.

3.6. Biocompatibility and Surface Morphology Analysis. Diamond is a biocompatible material, and studies have shown that diamond has minimal immune system response⁶⁰

and promotes cell adhesion and proliferation. As mentioned in the previous studies, a high concentration of diamond enhances cell growth and provides a compatible surface to promote osteoblast adhesion.⁶¹ TiD surfaces were oxygen-functionalized to activate the surface and enhance the biological response at the interface due to improved surface hydrophilicity. Consequently, this led to us studying their electrochemical behavior while considering their suitability for medical applications. Surface roughness has been reported to be critical to cell adhesion at the implant interface. With reference to Kurtosis ($x < 3$), both surfaces are considered (not sharp) and the surface features (unmelted particles) are considered squashed and round as shown in the SEM images (Figure 2) which enhances the cell viability on the surface.^{62,63}

Figure 7 displays healthy cells on both group A (TiD₅₀) and B (TiD₃₀) surfaces with neurites extrusion from the soma. TiD₅₀ has more cells without clustering compared to the sample with less diamond content, indicating a more biocompatible surface than TiD₃₀. While both the TiD samples had similar Rv (35.11 and 36.04 μm , respectively), TiD₅₀ has the highest Rp value (74.51 μm) compared to the Rp value (41.47 μm) of TiD₃₀. The TiD₃₀ sample provides a smoother surface compared to TiD₅₀, which is a potential reason for it displaying more neurites per neuron and longer neurites than TiD₅₀, as shown in the statistical analysis presented in Figure 8c–e. It is important to note that both the groups of TiD could support neuronal survival, although they exhibit different Cp and CIC values. Their CIC values (526 and 215 $\mu\text{C cm}^{-2}$) are comparable to nitrogen included ultrananocrystalline diamond (N-UNCD) with a CIC value of 1 mC cm^{-2} .⁶⁴ Overall, it becomes apparent that several factors affect the electrochemical behavior and cell viability of the TiD samples. It is

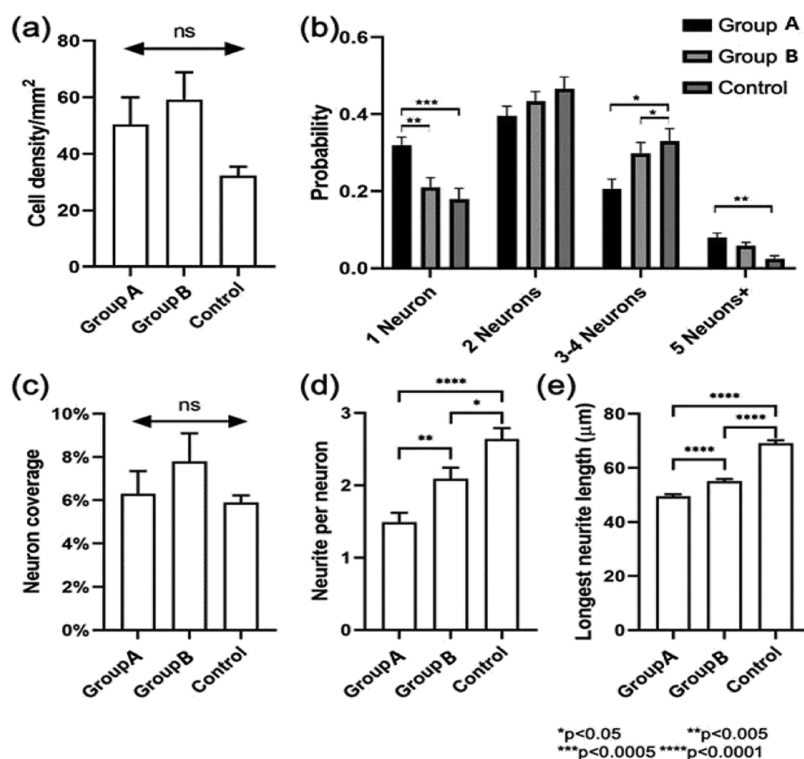


Figure 8. Summary of the quantified analysis of neurons on group A (TiD₅₀), B (TiD₃₀), and the control. The cell density, probability of cell clustering, neuron coverage, neurite per neuron, and the longest neurite length are shown in (a–e). Error bars represent the SEM. Number > 15. Statistical analysis was performed using Welch's *t*-test.

considered that the electrochemical behavior can be modulated by optimizing AM process according to the needed application by printing the needed surface morphology.

4. OUTLOOK

The findings reported here will prove helpful in expanding the possibilities to 3D print complex neural interfaces taking into account the individual geometric variation and anatomical diversity of the tissue.^{56,65} Moreover, the neural interfaces have suffered degradation and efficacy deterioration due to the body reaction at the tissue–electrode interface, and our research will provide the avenue to explore durable AM materials suitability for neural applications. Nevertheless, LMD will improve the engineering process by reducing the fabrication steps and addressing the need for custom-designed devices. For instance, the current configuration methods of coated electrodes require many pre-processing and post-processing steps and, more importantly, generate a lot of unused (waste) material. Previous literature demonstrates the long generic process of constructing diamond-coated arrays, starting with the substrate and ending with the exposed electrodes. This conventional fabrication method requires a long chain of intermediate steps to integrate diamond, treat the material, build diamond channels, and mask the unneeded material.^{66,67} On the other side, this paper presents the suggested model to 3D print diamond planar interfaces for neural applications, using minimal powder preparation, single-step fabrication step using the exact amount of material needed for the design, and, consequently, less residual waste.⁶⁸

5. CONCLUSIONS

This study is a preliminary investigation of the advanced functionality of TiD. We have demonstrated the feasibility of tuning the electrochemical properties of the TiD–electrolyte interface via optimizing the diamond concentration and surface modifications. The samples show high capacitance and require minimal post-processing to modulate their electrochemical behavior. The results confirm that the TiD behavior is influenced by various parameters, such as powder chemistry (diamond %), surface functionalization (oxygen functionalization), and morphology (roughness %). The C_p reached a value of $1053 \mu\text{F cm}^{-2}$ with a 50% diamond volume fraction with a CIC value of $526 \mu\text{C cm}^{-2}$. Moreover, the neural studies showed healthy cell growth on the TiD surface, confirming the material's non-cytotoxicity.

In conclusion, we present the properties of conductive planar TiD as an optimal model for electrode/interface studies. Owing to their reliable electrochemical behavior, selective surface properties, and scalability, the proposed fabrication model is envisioned to allow printing 3D architectures with the desired dimensions for different emergent applications in the neural interfacing and smart bio-sensing medical fields. Prior to this study, LMD has not been considered an electrode or conductive surface printing method. Here, we have presented its feasibility to print site-specific conductive surfaces in one step. Future work includes further investigation of the charge transfer mechanism, capacitance enhancement by different surface functionalization methods, and design optimization *via* AM.

■ ASSOCIATED CONTENT

Supporting Information

The Supporting Information is available free of charge at <https://pubs.acs.org/doi/10.1021/acsami.1c07318>.

EIS and Nyquist plots of the hybrid titanium–diamond material (PDF)

■ AUTHOR INFORMATION

Corresponding Author

Kate Fox – School of Engineering, RMIT University, Melbourne, Victoria 3001, Australia; Centre for Additive Manufacturing, RMIT University, Melbourne, Victoria 3001, Australia; orcid.org/0000-0001-8090-3215; Email: kate.fox@rmit.edu.au

Authors

Nour Mani – School of Engineering, RMIT University, Melbourne, Victoria 3001, Australia; Centre for Additive Manufacturing, RMIT University, Melbourne, Victoria 3001, Australia; orcid.org/0000-0001-8384-6578

Arman Ahnood – School of Engineering, RMIT University, Melbourne, Victoria 3001, Australia

Danli Peng – School of Physics, The University of Melbourne, Melbourne, Victoria 3010, Australia

Wei Tong – School of Physics, The University of Melbourne, Melbourne, Victoria 3010, Australia; National Vision Research Institute, Australian College of Optometry, Carlton, Victoria 3010, Australia

Marsilea Booth – School of Engineering, RMIT University, Melbourne, Victoria 3001, Australia

Alan Jones – Centre for Additive Manufacturing, RMIT University, Melbourne, Victoria 3001, Australia

Billy Murdoch – RMIT Microscopy and Microanalysis Facility, Melbourne, Victoria 3001, Australia; orcid.org/0000-0002-5875-2729

Nhiem Tran – School of Science, RMIT University, Melbourne, Victoria 3001, Australia; orcid.org/0000-0002-0209-2434

Shadi Houshyar – School of Engineering, RMIT University, Melbourne, Victoria 3001, Australia; orcid.org/0000-0003-0288-8608

Complete contact information is available at: <https://pubs.acs.org/doi/10.1021/acsami.1c07318>

Author Contributions

N.M.: sample preparation and characterization, visualization, formal analysis, investigation, conceptualization, and writing the original draft. W.T. and D.P.: characterization and formal analysis. A.J.: technical provision. M.B.: analysis and review. B.M.: review. N.T. and S.H.: supervision and review. K.F. and A.A.: writing—review, editing, supervision, conceptualization, and funding.

Notes

The authors declare no competing financial interest.

■ ACKNOWLEDGMENTS

The authors acknowledge the facilities and technical assistance of the RMIT Advanced Manufacturing Precinct. The authors also appreciate the access granted to the facilities and the scientific and technical assistance of the Australian Microscopy & Microanalysis Research Facility at RMIT University. S.H. acknowledges RMIT Vice-Chancellor Research Fellowship.

W.T. is supported by a University of Melbourne Early Career Researcher grant (2021ECR091). This work was supported by the Clive and Vera Ramaciotti Foundation and the CASS Foundation (Medicine and Science). K.F. also acknowledges the ARC for funding (IC160100026).

REFERENCES

- (1) Hatsopoulos, N. G.; Donoghue, J. P. The science of neural interface systems. *Annu. Rev. Neurosci.* **2009**, *32*, 249–266.
- (2) Aryan, N. P.; Kaim, H.; Rothermel, A. *Stimulation and Recording Electrodes for Neural Prostheses*, 1st ed.; Hans, K., Rothermel, A., Eds.; Springer: Cham, Germany, 2015.
- (3) Farina, D.; Vujaklija, I.; Brånemark, R.; Bull, A. M. J.; Diel, H.; Graimann, B.; Hargrove, L.; Hoffman, K.; Huang, H.; Ingvarsson, T.; Junusson, H.; Kristjansson, K.; Kuiken, T.; Micera, S.; Stieglitz, T.; Sturma, A.; Tyler, D.; Weir, R.; Aszmann, O. Toward higher-performance bionic limbs for wider clinical use. *Nat. Biomed. Eng.* **2021**, DOI: 10.1038/s41551-021-00732-x.
- (4) Trevisan, F.; Calignano, F.; Aversa, A.; Marchese, G.; Lombardi, M.; Biamino, S.; Ugues, D.; Manfredi, D. Additive manufacturing of titanium alloys in the biomedical field: processes, properties and applications. *J. Appl. Biomater. Funct. Mater.* **2018**, *16*, 57–67.
- (5) Ghilan, A.; Chiriac, A. P.; Nita, L. E.; Rusu, A. G.; Neamtu, I.; Chiriac, V. M. Trends in 3D Printing Processes for Biomedical Field: Opportunities and Challenges. *J. Polym. Environ.* **2020**, *28*, 1345–1367.
- (6) Ambrosi, A.; Pumera, M. 3D-printing technologies for electrochemical applications. *Chem. Soc. Rev.* **2016**, *45*, 2740–2755.
- (7) Froes, F. H.; Qian, M. *Titanium in Medical and Dental Applications*; Froes, F. H., Qian, M., Eds.; Woodhead Publishing: Duxford, United Kingdom, 2018.
- (8) Mani, N.; Sola, A.; Trinchi, A.; Fox, K. Is there a future for additive manufactured titanium bioglass composites in biomedical application? A perspective. *Biointerphases* **2020**, *15*, 068501.
- (9) Kozai, T. D. Y.; Catt, K.; Li, X.; Gugel, Z. V.; Olafsson, V. T.; Vazquez, A. L.; Cui, X. T. Mechanical failure modes of chronically implanted planar silicon-based neural probes for laminar recording. *Biomaterials* **2015**, *37*, 25–39.
- (10) Fox, K.; Mani, N.; Rifai, A.; Reineck, P.; Jones, A.; Tran, P. A.; Ramezannejad, A.; Brandt, M.; Gibson, B. C.; Greentree, A. D.; Tran, N. 3D-Printed Diamond–Titanium Composite: A Hybrid Material for Implant Engineering. *ACS Appl. Bio Mater.* **2020**, *3*, 29–36.
- (11) Yang, N.; Yu, S.; Macpherson, J. V.; Einaga, Y.; Zhao, H.; Zhao, G.; Swain, G. M.; Jiang, X. Conductive diamond: synthesis, properties, and electrochemical applications. *Chem. Soc. Rev.* **2019**, *48*, 157–204.
- (12) Mani, N.; Rifai, A.; Houshyar, S.; Booth, M. A.; Fox, K. Diamond in medical devices and sensors: An overview of diamond surfaces. *Med. Devices Sens.* **2020**, *3*, No. e10127.
- (13) McCreery, R. L. Advanced Carbon Electrode Materials for Molecular Electrochemistry. *Chem. Rev.* **2008**, *108*, 2646–2687.
- (14) Luong, J. H. T.; Male, K. B.; Glennon, J. D. Boron-doped diamond electrode: synthesis, characterization, functionalization and analytical applications. *Analyst* **2009**, *134*, 1965–1979.
- (15) Guo, X.; Wang, Y.; Wang, X.; Xi, X.; Gu, Y.; Liu, Q.; Li, Y.; Li, J. Nitrogen-doped nanodiamond films grown just by heating solid precursor thin layers for field emission application. *J. Phys. D: Appl. Phys.* **2019**, *53*, 015101.
- (16) Zhang, R.; Pu, J.; Yang, Y.; Guo, L.; Wang, J. Probing the frictional properties of sulfur-doped diamond-like carbon films under high vacuum by first-principles calculations. *Appl. Surf. Sci.* **2019**, *481*, 1483–1489.
- (17) Fabisiak, K.; Torz-Piotrowska, R.; Stryga, E.; Szybowicz, M.; Paprocki, K.; Popielarski, P.; Bylicki, F.; Wrzyszczyński, A. Cyclic voltammetry response of an undoped CVD diamond electrodes. *J. Mater. Sci. Eng. B* **2012**, *177*, 1243–1247.
- (18) Kowalska, M.; Paprocki, K.; Szybowicz, M.; Wrzyszczyński, A.; Łoś, S.; Fabisiak, K. Electrochemical sensitivity of undoped CVD diamond films as function of their crystalline quality. *J. Electroanal. Chem.* **2020**, *859*, 113811.
- (19) Szunerits, S.; Boukherroub, R. Different strategies for functionalization of diamond surfaces. *J. Solid State Electrochem.* **2007**, *12*, 1205–1218.
- (20) Salvadori, M. C.; Araújo, W. W. R.; Teixeira, F. S.; Cattani, M.; Pasquarelli, A.; Oks, E. M.; Brown, I. G. Termination of diamond surfaces with hydrogen, oxygen and fluorine using a small, simple plasma gun. *Diamond Relat. Mater.* **2010**, *19*, 324–328.
- (21) Mayrhofer, L.; Moras, G.; Mulakaluri, N.; Rajagopalan, S.; Stevens, P. A.; Moseler, M. Fluorine-Terminated Diamond Surfaces as Dense Dipole Lattices: The Electrostatic Origin of Polar Hydrophobicity. *J. Am. Chem. Soc.* **2016**, *138*, 4018–4028.
- (22) Rezek, B.; Kratka, M.; Ukraintsev, E.; Babchenko, O.; Kromba, A.; Broz, A.; Kalbacova, M. Diamond as Functional Material for Bioelectronics and Biotechnology. *New Perspectives in Biosensors Technology and Applications*; Intech, 2011; pp 177–196.
- (23) Voss, A.; Stateva, S. R.; Reithmaier, J. P.; Apostolova, M. D.; Popov, C. Patterning of the surface termination of ultrananocrystalline diamond films for guided cell attachment and growth. *Surf. Coat. Technol.* **2017**, *321*, 229–235.
- (24) Navas, J.; Araujo, D.; Piñero, J. C.; Sánchez-Coronilla, A.; Blanco, E.; Villar, P.; Alcántara, R.; Montserrat, J.; Florentin, M.; Eon, D.; Pernot, J. Oxygen termination of homoepitaxial diamond surface by ozone and chemical methods: An experimental and theoretical perspective. *Appl. Surf. Sci.* **2018**, *433*, 408–418.
- (25) Araujo, W. W. R.; Teixeira, F. S.; Da Silva, G. N.; Salvadori, D. M. F.; Salvadori, M. C. Cell adhesion and growth on surfaces modified by plasma and ion implantation. *J. Appl. Phys.* **2014**, *115*, 154701.
- (26) Duailibi, S. E.; Duailibi, M. T.; Ferreira, L. M.; Salmazi, K. I. L. C.; Salvadori, M. C.; Teixeira, F. D. S.; Pasquarelli, A.; Vacanti, J. P.; Yelick, P. C. Tooth tissue engineering: The influence of hydrophilic surface on nanocrystalline diamond films for human dental stem cells. *Tissue Eng., Part A* **2013**, *19*, 2537–2543.
- (27) Childres, I.; Jauregui, L. A.; Tian, J.; Chen, Y. P. Effect of oxygen plasma etching on graphene studied using Raman spectroscopy and electronic transport measurements. *New J. Phys.* **2011**, *13*, 025008.
- (28) Brown, N. M. D.; Cui, N.; McKinley, A. A study of the topography of a glassy carbon surface following low-power radio-frequency oxygen plasma treatment. *Appl. Surf. Sci.* **1998**, *133*, 157–165.
- (29) Gulzar, U.; Glynn, C.; O'Dwyer, C. Additive manufacturing for energy storage: Methods, designs and material selection for customizable 3D printed batteries and supercapacitors. *Curr. Opin. Electrochem.* **2020**, *20*, 46–53.
- (30) Tong, W.; Fox, K.; Zamani, A.; Turnley, A. M.; Ganesan, K.; Ahnood, A.; Cicione, R.; Meffin, H.; Praver, S.; Stacey, A.; Garrett, D. J. Optimizing growth and post treatment of diamond for high capacitance neural interfaces. *Biomaterials* **2016**, *104*, 32–42.
- (31) Bard, A. J.; Faulkner, L. R. *Electrochemical Methods: Fundamentals and Applications*, New York: Wiley, 2001, 2nd ed. *Russ. J. Electrochem.* **2002**, *38*, 1364–1365.
- (32) Haas, A. J.; Prigent, S.; Dutertre, S.; Le Dréan, Y.; Le Page, Y. Neurite analyzer: An original Fiji plugin for quantification of neuritogenesis in two-dimensional images. *J. Neurosci. Methods* **2016**, *271*, 86–91.
- (33) Su, X.; Yang, Y. Research on track overlapping during Selective Laser Melting of powders. *J. Mater. Process. Technol.* **2012**, *212*, 2074–2079.
- (34) Zhu, Z.; Lou, S.; Majewski, C. Characterisation and correlation of areal surface texture with processing parameters and porosity of High Speed Sintered parts. *Addit. Manuf.* **2020**, *36*, 101402.
- (35) Duan, X.; Tian, W.; Zhang, H.; Sun, H.; Ao, Z.; Shao, Z.; Wang, S. sp²/sp³ Framework from Diamond Nanocrystals: A Key Bridge of Carbonaceous Structure to Carbocatalysis. *ACS Catal.* **2019**, *9*, 7494–7519.

- (36) Osswald, S.; Yushin, G.; Mochalin, V.; Kucheyev, S. O.; Gogotsi, Y. Control of sp²/sp³ Carbon Ratio and Surface Chemistry of Nanodiamond Powders by Selective Oxidation in Air. *J. Am. Chem. Soc.* **2006**, *128*, 11635–11642.
- (37) Shenderova, O.; Koscheev, A.; Zaripov, N.; Petrov, I.; Skryabin, Y.; Detkov, P.; Turner, S.; Van Tendeloo, G. Surface Chemistry and Properties of Ozone-Purified Detonation Nanodiamonds. *J. Phys. Chem. C* **2011**, *115*, 9827–9837.
- (38) Fox, K.; Mani, N.; Rifai, A.; Reineck, P.; Jones, A.; Tran, P. A.; Ramezannejad, A.; Brandt, M.; Gibson, B. C.; Greentree, A. D.; Tran, N. 3D-Printed Diamond–Titanium Composite: A Hybrid Material for Implant Engineering. *ACS Appl. Bio Mater.* **2019**, *3*, 29–36.
- (39) Liu, F. B.; Jing, B.; Cui, Y.; Di, J. J.; Qu, M. Voltammetric and impedance behaviours of surface-treated nano-crystalline diamond film electrodes. *AIP Adv.* **2014**, *5*, 041306.
- (40) Ho-Yin Chan, H.; Aslam, D. M.; Wiler, J. A.; Casey, B. A Novel Diamond Microprobe for Neuro-Chemical and -Electrical Recording in Neural Prosthesis. *J. Microelectromech. Syst.* **2009**, *18*, 511–521.
- (41) Weiland, J. D.; Anderson, D. J.; Humayun, M. S. In vitro electrical properties of iridium oxide versus titanium nitride stimulating electrodes. *IEEE Trans. Biomed. Eng.* **2002**, *49*, 1574–1579.
- (42) Chambers, A.; Ahnood, A.; Falahatdoost, S.; Yianni, S.; Hoxley, D.; Johnson, B. C.; Garrett, D. J.; Tomljenovic-Hanic, S.; Prawer, S. Near-infrared excitation of nitrogen-doped ultrananocrystalline diamond photoelectrodes in saline solution. *Diamond Relat. Mater.* **2020**, *103*, 107720.
- (43) Merrill, D. R.; Bikson, M.; Jefferys, J. G. R. Electrical stimulation of excitable tissue: design of efficacious and safe protocols. *J. Neurosci. Methods* **2005**, *141*, 171–198.
- (44) Kumsa, D. W.; Bhadra, N.; Hudak, E. M.; Kelley, S. C.; Untereker, D. F.; Mortimer, J. T. Electron transfer processes occurring on platinum neural stimulating electrodes: a tutorial on the *i*(V) *e* profile. *J. Neural Eng.* **2016**, *13*, 052001.
- (45) Cogan, S. F.; Troyk, P. R.; Ehrlich, J.; Plante, T. D. In vitro comparison of the charge-injection limits of activated iridium oxide (AIROF) and platinum-iridium microelectrodes. *IEEE Trans. Biomed. Eng.* **2005**, *52*, 1612–1614.
- (46) Cui, H.; Xie, X.; Xu, S.; Chan, L. L. H.; Hu, Y. Electrochemical characteristics of microelectrode designed for electrical stimulation. *BioMed. Eng. Online* **2019**, *18*, 86.
- (47) Yang, K.-H.; Narayan, R. J. Biocompatibility and functionalization of diamond for neural applications. *Curr. Opin. Biomed. Eng.* **2019**, *10*, 60–68.
- (48) Popov, K. M.; Fedoseeva, Y. V.; Kokhanovskaya, O. A.; Razz'yakonova, G. I.; Smirnov, D. A.; Bulusheva, L. G.; Okotrub, A. V. Functional composition and electrochemical characteristics of oxidized nanosized carbon. *J. Struct. Chem.* **2017**, *58*, 1187–1195.
- (49) Dulyaseree, P.; Yordsri, V.; Wongwiriyan, W. Effects of microwave and oxygen plasma treatments on capacitive characteristics of supercapacitor based on multiwalled carbon nanotubes. *Jpn. J. Appl. Phys.* **2016**, *55*, 02BD05.
- (50) Plana, D.; Humphrey, J. J. L.; Bradley, K. A.; Celorrio, V.; Fermín, D. J. Charge Transport Across High Surface Area Metal/Diamond Nanostructured Composites. *ACS Appl. Mater. Interfaces* **2013**, *5*, 2985–2990.
- (51) Cogan, S. F. Neural Stimulation and Recording Electrodes. *Annu. Rev. Biomed. Eng.* **2008**, *10*, 275–309.
- (52) Wang, R.; Lang, J.; Yan, X. Effect of surface area and heteroatom of porous carbon materials on electrochemical capacitance in aqueous and organic electrolytes. *Sci. China: Chem.* **2014**, *57*, 1570–1578.
- (53) Zhang, L.; Yang, X.; Zhang, F.; Long, G.; Zhang, T.; Leng, K.; Zhang, Y.; Huang, Y.; Ma, Y.; Zhang, M.; Chen, Y. Controlling the Effective Surface Area and Pore Size Distribution of sp² Carbon Materials and Their Impact on the Capacitance Performance of These Materials. *J. Am. Chem. Soc.* **2013**, *135*, 5921–5929.
- (54) Meijs, S.; McDonald, M.; Sørensen, S.; Rechendorff, K.; Fekete, L.; Klimša, L.; Petrak, V.; Rijkhoff, N.; Taylor, A.; Nesladek, M.; Pennisi, C. P. Diamond/Porous Titanium Nitride Electrodes with Superior Electrochemical Performance for Neural Interfacing. *Front. Bioeng. Biotechnol.* **2018**, *6*, 171.
- (55) Ye, H.; Hing, P. Dielectric Behavior of Diamond Films. *Int. J. Thermophys.* **2001**, *22*, 1285–1294.
- (56) Luan, L.; Robinson, J. T.; Aazhang, B.; Chi, T.; Yang, K.; Li, X.; Rathore, H.; Singer, A.; Yellapantula, S.; Fan, Y.; Yu, Z.; Xie, C. Recent Advances in Electrical Neural Interface Engineering: Minimal Invasiveness, Longevity, and Scalability. *Neuron* **2020**, *108*, 302–321.
- (57) McCreery, D. B.; Agnew, W. F.; Yuen, T. G. H.; Bullara, L. Charge density and charge per phase as cofactors in neural injury induced by electrical stimulation. *IEEE Trans. Biomed. Eng.* **1990**, *37*, 996–1001.
- (58) Shoar Abouzari, M. R.; Berkemeier, F.; Schmitz, G.; Wilmer, D. On the physical interpretation of constant phase elements. *Solid State Ionics* **2009**, *180*, 922–927.
- (59) Randviir, E. P.; Banks, C. E. Electrochemical impedance spectroscopy: an overview of bioanalytical applications. *Anal. Methods* **2013**, *5*, 1098–1115.
- (60) Garrett, D. J.; Tong, W.; Simpson, D. A.; Meffin, H. Diamond for neural interfacing: A review. *Carbon* **2016**, *102*, 437–454.
- (61) Fox, K.; Ratwatte, R.; Booth, M. A.; Tran, H. M.; Tran, P. A. High Nanodiamond Content-PCL Composite for Tissue Engineering Scaffolds. *Nanomater.* **2020**, *10*, 948.
- (62) Shaoki, A.; Xu, J.-y.; Sun, H.; Chen, X.-s.; Ouyang, J.; Zhuang, X.-M.; Deng, F.-L. Osseointegration of three-dimensional designed titanium implants manufactured by selective laser melting. *Biofabrication* **2016**, *8*, 045014.
- (63) Shim, J.; Nakamura, H.; Ogawa, T.; Gupta, V. An Understanding of the Mechanism That Promotes Adhesion Between Roughened Titanium Implants and Mineralized Tissue. *J. Biomech. Eng.* **2009**, *131*, 054503.
- (64) Garrett, D. J.; Ganesan, K.; Stacey, A.; Fox, K.; Meffin, H.; Prawer, S. Ultra-nanocrystalline diamond electrodes: optimization towards neural stimulation applications. *J. Neural Eng.* **2012**, *9*, 016002.
- (65) Mahamood, R. M. *Laser Metal Deposition Process of Metals, Alloys, and Composite Materials*; Derby, B., Ed.; Springer International Publishing: Cham, 2018.
- (66) Piret, G.; Hébert, C.; Mazellier, J.-P.; Rousseau, L.; Scorsone, E.; Cottance, M.; Lissorgues, G.; Heuschkel, M. O.; Picaud, S.; Bergonzo, P.; Yvert, B. 3D-nanostructured boron-doped diamond for microelectrode array neural interfacing. *Biomaterials* **2015**, *53*, 173–183.
- (67) Pippione, G.; Olivero, P.; Fischer, M.; Schreck, M.; Pasquarelli, A. Characterization of CVD Heavily B-Doped Diamond Thin Films for Multi Electrode Array Biosensors. *Phys. Status Solidi A* **2017**, *214*, 1700223.
- (68) Mani, M.; Lyons, K. W.; Gupta, S. K. Sustainability Characterization for Additive Manufacturing. *J. Res. Natl. Inst. Stand. Technol.* **2014**, *119*, 419–428.